Modeling and analysis of a dual-acoustic-driver thermoacoustic heat pump

Geng Chen[1, *], Lihua Tang[2], Zhibin Yu[3]

1. National Engineering Research Center of Power Generation Control and Safety, School of Energy and Environment, Southeast University, Nanjing 210096, China
2. Department of Mechanical Engineering, University of Auckland, Auckland 1010, New Zealand
3. James Watt School of Engineering, University of Glasgow, Glasgow G12 8QQ, UK

ABSTRACT

Thermoacoustic heat pumps (TAHPs) can be used for heating and/or cooling purposes. Current designs of travelling-wave TAHPs normally employ a single acoustic driver and rely on a looped pipe to establish and maintain the required acoustic field. The resultant system is thereby bulky and expensive, detracting from the structure simplicity and low-cost advantages of thermoacoustic technology. To address this issue, this paper investigates the dual-acoustic-driver concept that can significantly increase the system's compactness. Theoretical analyses are conducted for the dual-acoustic-driver TAHP, and the acoustic and temperature fields in the thermoacoustic core are examined. Parametric studies are undertaken to investigate the effects of acoustic drivers on the acoustic and thermal characteristics of the TAHP. It is found that, as the frequency of acoustic drivers changes, the acoustic field in the thermoacoustic (TA) core could be dominated by a standing, traveling, or hybrid standing-traveling wave. The temperature distribution within the TA core and temperature difference between the core ends will change accordingly. Results show that the temperature difference is non-zero only when the acoustic field contains a traveling-wave component. To obtain a large temperature difference, the acoustic drivers should be driven near resonance frequencies at which the acoustic field is hybrid and the pressure amplitude is large. This study gains new insights into the working mechanisms behind the dual-acoustic-driver TAHP concept, paving the way for developing compact, efficient, and high-power-density TAHPs for industrial waste heat recovery.

Keywords: Thermoacoustic heat pump; Dual-acoustic-driver; Thermoacoustic core; Hybrid standing-traveling wave; Waste heat recovery;

[*] Correspondent author: chengeng@seu.edu.cn

Nomenclature

c	speed of sound (m/s)	*Greek symbols*	
c_p	isobaric specific heat (J/kgK)	θ_{pU}	phase difference between p and U (°)
D	diameter (m)	δ_v	viscous penetration depth (m)
d	displacement amplitude (m)	δ_k	thermal penetration depth (m)
f	frequency (Hz)	κ_{solid}	thermal conductivity of solid (W/mK)
$f_{v,k}$	thermal-viscous functions	ρ	density (kg/m^3)
G	standing-wave ratio	ϕ_{AB}	phase difference between A and B (°)
$h_{v,k}$	thermal-viscous functions	ω	frequency (rad/s)
j	$\sqrt{-1}$		
k	wavenumber	*Subscripts*	
L	duct length (m)	*Max*	maximum
L_H	heat exchanger length (m)	*Min*	minimum
L_S	thermoacoustic core length (m)	*SW*	standing wave
t_S	thermoacoustic core thickness (m)	*TW,L*	left-propagating traveling wave
d_S	gap between plates (m)	*TW,R*	right-propagating traveling wave
p	acoustic pressure (Pa)		
Pr	Prandtl number	*Abbreviations*	
S	cross-sectional area of fluid (m^2)	$\Re[\ ]$	real part of a complex quantity
S_{solid}	cross-sectional area of solid (m^2)	$\Im[\ ]$	imaginary part of a complex quantity
s	entropy (J/kgK)	HE	heat exchanger
T	temperature (K)	TA	thermoacoustic
U	volume velocity (m^3/s)	TAR	thermoacoustic refrigerator
u	velocity (m/s)	TAHP	thermoacoustic heat pump

1. Introduction

The depletion of fossil fuels and the associated environmental impact have driven a growing interest in increasing energy efficiency and exploiting renewable energy sources. However, a large amount of untapped heat (below 100 °C) is wasted in the industry. Recovering the low-grade industrial waste heat is critical for addressing the energy-related problems such as energy shortage and greenhouse gas emission in the global world [1]. Thermoacoustic technology, an emerging technology, offers a new approach for exploiting industrial waste heat either through a thermoacoustically-driven thermoacoustic refrigerator

(TAR) that utilizes the low-grade heat to produce refrigeration [2] or through a thermoacoustic heat pump (TAHP) that upgrades the low-grade heat to high-grade heat at the cost of external work [3].

TARs or TAHPs are attractive due to their minimum use of moving components and relatively benign environmental impact (by using noble and inert gases) [4-6]. In TARs or TAHPs, an acoustic wave in the compressible fluid is first generated and propagates along the waveguide. Interactions between the oscillatory fluid and solid stack/regenerator (i.e., a piece of porous material) lead to a hydrodynamic heat pumping effect that transports heat within the fluid boundary layers in the direction of wave propagation [7]. The thermoacoustic heat pumping effect was first observed by Merkli [8] in a standing-wave TAR driven by an oscillating piston in 1975. Thereafter, Wheatley [9], Hofler [10], Swift [11], etc. conducted a series of experimental studies on standing-wave TARs and used the linear thermoacoustic theory [12] to estimate the TAR performance. The prototype of a traveling-wave TAR, which demonstrated a smaller onset temperature compared with its standing-wave counterpart, was first constructed by Yazaki [13] in 2002. Following his study, Tijani [14], Luo [15], De Blok [16], etc. made great progress in the development of traveling-wave TARs.

After 2-3 decades of research efforts, travelling-wave TARs or TAHPs have advanced significantly to the point of viable commercial applications. Sound Energy Ltd [17] in the Netherlands has launched a solar thermally powered thermoacoustic cooler system for air conditioning. The first product has been successfully installed in Saudi Arabia. However, there are still several technical obstacles hindering the wide commercialization of TAHPs, among which is the structure complexity. Traditional standing-wave TARs (or TAHPs) own a simple structure by using a linear pipe called an “acoustic resonator” [18-20]. However, due to the irreversibility resulting from imperfect heat transfer between the oscillatory fluid and stack, the heat pumping capacity of those devices is typically very low [21]. Traditional travelling-wave TARs (or TAHPs) are more efficient in energy conversion by using a looped pipe that facilitates a traveling wave [22-24]. Nonetheless, compared with the resonator, the loop adds structure complexity, occupies more space, and increases the construction cost. Therefore, it is important to develop a new topology to improve the compactness and heat pumping capacity of the TAR or TAHP.

To address the challenge stated above, a dual-acoustic-driver concept was proposed by Poignand [25, 26] in 2011. A coaxial, compact TAHP was built that provided compactness and flexibility compared to classical thermoacoustic devices. In 2016, Widyaparaga [27, 28] experimentally studied a TAHP driven by two loudspeakers. By altering the magnitude and phase difference of loudspeakers, the heat pumping direction along the regenerator was seen to change and reverse. In 2020, El-Rahman et al. [29] constructed a TAR driven by two pistons powered by a rotary motor. The TAR operated at 42 Hz and produced a temperature difference of 27 K. Recently, Ramadan [30] manufactured a TAR similar to

Poignand's design but with a higher cooling capacity. In summary, the existing studies in the literature have demonstrated that the dual-acoustic-driver concept can improve the compactness of the TAR or TAHP while maintaining a comparable heat pumping capacity with traditional single-acoustic-driver thermoacoustic devices. However, previous studies mostly focused on experimental trials and their results are random. Few theoretical studies on dual-acoustic-driver TARs or TAHPs were reported. The underlying mechanisms of thermoacoustic heat pumping by two acoustic drivers are still less clear.

This study aims at exploring the working mechanisms of a dual-acoustic-driver TAHP from both acoustic and thermodynamic viewpoints. The acoustic and temperature fields within the TAHP are analyzed theoretically. The effects of acoustic drivers on the heat pumping performance are examined. The remainder of the paper is divided into four sections. Section 2 introduces the dual-acoustic-driver TAHP investigated in this study. Section 3 describes and analyzes the acoustic characteristics of the TAHP. Section 4 elaborates on the thermal characteristics of the TAHP. Finally, concluding remarks are drawn in Section 5.

2. Problem statement

2.1 Model description

Figure 1 shows the schematic of the dual-acoustic-driver thermoacoustic heat pump (TAHP) investigated in this study. It consists of a thermoacoustic (TA) core that is made of thin metal sheets with a parallel-plate structure, a pair of heat exchangers (HEs), a linear duct in which the acoustic waves propagate, and two acoustic drivers (depicted as solid pistons A and B) at the duct ends. The working fluid inside the system could be helium or other noble gases. The acoustic drivers could be solid pistons, linear alternators, loudspeakers, piezoelectric actuators, etc., depending on the size of the device, construction cost, or cooling demand [31-33]. In this research, we denote the parallel-plate structure as "TA core" instead of "stack" or "regenerator" since the acoustic field inside often contains both standing- and traveling-wave components. For simplicity, the working fluid is chosen as air at atmospheric pressure and temperature (i.e., 101,325 Pa and 300 K) while the TA core is made of carbon steel. The two acoustic drivers operate sinusoidally at the same driving frequency f and displacement amplitude ($d_A = d_B$) but with a phase difference ϕ_{AB}. For example, when $\phi_{AB} = 0$, the two drivers will reach the leftmost and rightmost positions at the same time. In this study, f and ϕ_{AB} of the acoustic drivers are two control parameters (or variables) while the geometrical parameters of the TAHP are fixed, as listed in Table 1.

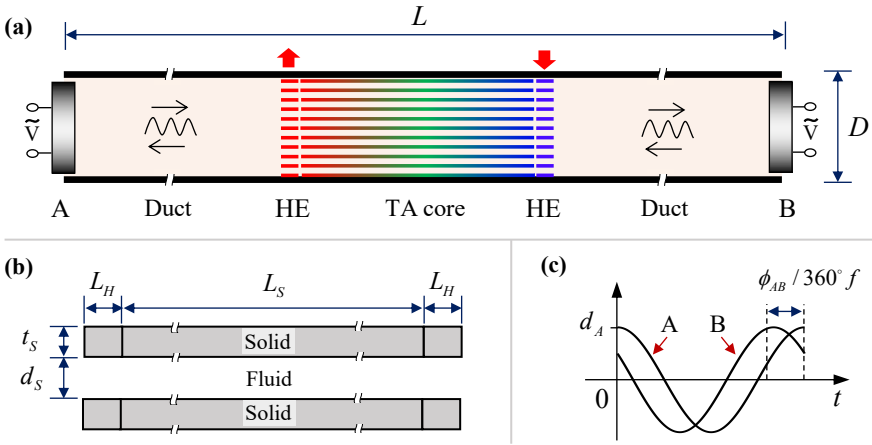

Figure 1. (a) Schematic of the dual-acoustic-driver TAHP. HE and TA core stand for heat exchanger and thermoacoustic core. A and B are two acoustic drivers. (b) Two adjacent plates. (c) Displacements of the two acoustic drivers.

Table 1. Key parameters of the benchmark model.

Components	**Parameters**	**Values and units**
Duct	Diameter D	0.02 m
	Length L	0.5 m
Heat exchangers	Length L_H	0.01 m
Thermoacoustic core	Length L_S	0.1 m
	Thickness t_S	1×10^{-4} m
	Gap between plates d_S	1×10^{-4} m
	Thermal conductivity κ_{solid}	50 W/(mK)
Acoustic drivers	Displacement amplitude d_A	0.001 m
	Displacement amplitude d_B	0.001 m

2.2 Working principle

Following the reciprocating acoustic drivers, the working fluid inside the TAHP becomes oscillatory. As such, the near-wall gas parcel between the plates inside the TA core contracts and expands while releasing and absorbing heat from the nearby plate at the same time (see Figure 2(a)). Therefore, a thermoacoustic heat pump (or refrigeration) cycle is formed, as seen in the shaded area in Figure 2(b). Accordingly, heat is pumped from one end of the core to the other, and the temperature of one heat exchanger will be higher than the other. If the hot heat exchanger is fixed at the ambient temperature, the device will function as a refrigerator (or cooler). If the cold heat exchanger is fixed at the ambient temperature, the device will function as a heat pump.

It should be stressed that the dual-acoustic-driver TAHP in this research is different from traditional Stirling heat pumps (or refrigerators) in the following two aspects. (1) Acoustic resonance. The TAHP relies on acoustic drivers and acoustic waveguides (i.e., linear duct) to adjust the acoustic field in the TA core. In particular, acoustic resonance is pursued (as will be discussed in Section 4) to obtain higher pressure amplitudes, and the driving frequency may reach several hundred Hz depending on the geometry of acoustic waveguides. In contrast, the acoustic field in Stirling heat pumps is only controlled by the displacement and phase angle of pistons which normally oscillate at 50 Hz to be consistent with the electric motors. In other words, Stirling heat pumps usually work at non-resonant states. (2) Thermodynamic cycles. The study of Stirling heat pumps is based on equilibrium thermodynamics. Ideally, there is a negligible temperature difference between the gas and regenerator, and the thermodynamic processes are reversible (see dashed lines in Figure 2(b)). However, the TAHP operates at non-equilibrium states due to the high driving frequency and there is always a thermal lag between the oscillatory fluid and solid TA core. For the TA core in a standing wave, the thermal lag has an optimal value, and the thermodynamic cycle resembles Brayton cycles [11]. For the TA core in a travelling wave, the thermal lag should be as small as possible so that the thermodynamic cycle will approach more-efficient Stirling cycles [34].

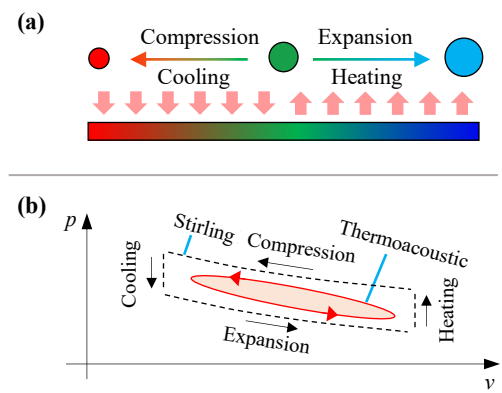

Figure 2. Working principle of the TAHP. (a) Heat pumping effect. (b) p - v diagrams of heat pump (or refrigeration) cycles.

3. Acoustic analysis

This section first explores the acoustic characteristics of the dual-acoustic-driver TAHP. The validation of the theoretical model established in this section can be found in Appendix A. The acoustic analysis in this section lays the foundation for the thermodynamic analysis in Section 4.

3.1 Simplified acoustic model

Figure 3 displays the simplified acoustic model of the dual-acoustic-driver TAHP. Acoustic drivers A and B are located at $x = 0$ and L, respectively. In the figure, $x_a = L/2 - L_S/2 - L_H$, $x_b = L/2 - L_S/2$, $x_c = L/2 + L_S/2$ and $x_d = L/2 + L_S/2 + L_H$, with L, L_S, L_H being the length of the entire device, TA core and heat exchangers.

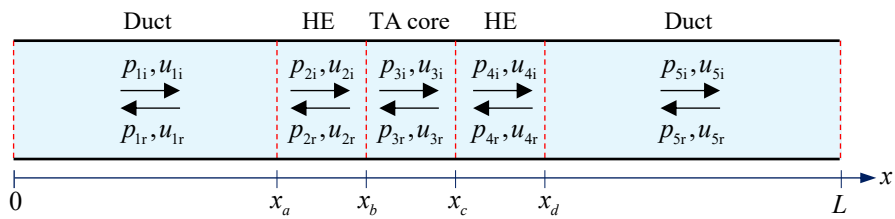

Figure 3. Simplified acoustic model of the dual-acoustic-driver TAHP. Acoustic drivers A and B locate at $x = 0$ and $x = L$.

Assume the propagation of acoustic waves in each part is lossless and one-dimensional. Thus, the acoustic pressure and velocity (in complex form) in each part are expressed by

$$
\begin{cases} p = p_{1\mathrm{i}} + p_{1\mathrm{r}} = p_{1\mathrm{ia}} e^{j(\omega t - kx)} + p_{1\mathrm{ra}} e^{j(\omega t + kx)} \\ u = u_{1\mathrm{i}} + u_{1\mathrm{r}} = u_{1\mathrm{ia}} e^{j(\omega t - kx)} + u_{1\mathrm{ra}} e^{j(\omega t + kx)} \end{cases}, 0 \le x \le x_a
$$

$$
\begin{cases} p = p_{2\mathrm{i}} + p_{2\mathrm{r}} = p_{2\mathrm{ia}} e^{j(\omega t - kx)} + p_{2\mathrm{ra}} e^{j(\omega t + kx)} \\ u = u_{2\mathrm{i}} + u_{2\mathrm{r}} = u_{2\mathrm{ia}} e^{j(\omega t - kx)} + u_{2\mathrm{ra}} e^{j(\omega t + kx)} \end{cases}, x_a \le x \le x_b
$$

$$
\begin{cases} p = p_{3\mathrm{i}} + p_{3\mathrm{r}} = p_{3\mathrm{ia}} e^{j(\omega t - kx)} + p_{3\mathrm{ra}} e^{j(\omega t + kx)} \\ u = u_{3\mathrm{i}} + u_{3\mathrm{r}} = u_{3\mathrm{ia}} e^{j(\omega t - kx)} + u_{3\mathrm{ra}} e^{j(\omega t + kx)} \end{cases}, x_b \le x \le x_c \tag{1}
$$

$$
\begin{cases} p = p_{4\mathrm{i}} + p_{4\mathrm{r}} = p_{4\mathrm{ia}} e^{j(\omega t - kx)} + p_{4\mathrm{ra}} e^{j(\omega t + kx)} \\ u = u_{4\mathrm{i}} + u_{4\mathrm{r}} = u_{4\mathrm{ia}} e^{j(\omega t - kx)} + u_{4\mathrm{ra}} e^{j(\omega t + kx)} \end{cases}, x_c \le x \le x_d
$$

$$
\begin{cases} p = p_{5\mathrm{i}} + p_{5\mathrm{r}} = p_{5\mathrm{ia}} e^{j(\omega t - kx)} + p_{5\mathrm{ra}} e^{j(\omega t + kx)} \\ u = u_{5\mathrm{i}} + u_{5\mathrm{r}} = u_{5\mathrm{ia}} e^{j(\omega t - kx)} + u_{5\mathrm{ra}} e^{j(\omega t + kx)} \end{cases}, x_d \le x \le L
$$

where $k = \omega/c$ denotes the wavenumber and c is the speed of sound. Subscripts "i" and "r" stand for the incident and reflected waves propagating in positive and negative directions, while subscript "a" denotes the amplitude of complex quantities. In Equation (1), the amplitudes of complex acoustic pressure and velocity in each part satisfy

$$\begin{cases} u_{1\text{ia}} = p_{1\text{ia}} / \rho c;\ u_{1\text{ra}} = -p_{1\text{ra}} / \rho c; \\ u_{2\text{ia}} = p_{2\text{ia}} / \rho c;\ u_{2\text{ra}} = -p_{2\text{ra}} / \rho c; \\ u_{3\text{ia}} = p_{3\text{ia}} / \rho c;\ u_{3\text{ra}} = -p_{3\text{ra}} / \rho c; \\ u_{4\text{ia}} = p_{4\text{ia}} / \rho c;\ u_{4\text{ra}} = -p_{4\text{ra}} / \rho c; \\ u_{5\text{ia}} = p_{5\text{ia}} / \rho c;\ u_{5\text{ra}} = -p_{5\text{ra}} / \rho c; \end{cases} \tag{2}$$

where ρ denotes the density. The acoustic boundary condition at $x = 0$ is

$$u_{1\text{ia}} + u_{1\text{ra}} = j\omega d_A \tag{3}$$

where d_A is the displacement amplitude of acoustic driver A. Equation (3) gives

$$p_{1\text{ra}} = p_{1\text{ia}} - j\omega d_A \rho c \tag{4}$$

Continuity of acoustic pressure and volume velocity (product of velocity and area) at $x = x_a$ gives

$$\begin{cases} p_{1\text{ia}} e^{-jkx_a} + p_{1\text{ra}} e^{jkx_a} = p_{2\text{ia}} e^{-jkx_a} + p_{2\text{ra}} e^{jkx_a} \\ \left(u_{1\text{ia}} e^{-jkx_a} + u_{1\text{ra}} e^{jkx_a}\right) S_1 = \left(u_{2\text{ia}} e^{-jkx_a} + u_{2\text{ra}} e^{jkx_a}\right) S_2 \end{cases} \tag{5}$$

where S_1 and S_2 are cross-sectional areas of the duct and TA core. Substitution of Equation (2) into Equation (5) yields

$$\begin{cases} p_{2\text{ia}} = \dfrac{\left(1 + S_1 / S_2\right) p_{1\text{ia}} e^{-jkx_a} + \left(1 - S_1 / S_2\right) p_{1\text{ra}} e^{jkx_a}}{2e^{-jkx_a}} \\ p_{2\text{ra}} = \dfrac{\left(1 - S_1 / S_2\right) p_{1\text{ia}} e^{-jkx_a} + \left(1 + S_1 / S_2\right) p_{1\text{ra}} e^{jkx_a}}{2e^{jkx_a}} \end{cases} \tag{6}$$

where $S_1/S_2 \approx (t_S + d_S)/d_S$, with t_S and d_S being the plate thickness and the gap between plates, respectively. Likewise, continuity of acoustic pressure and volume velocity at $x = x_b$ gives

$$\begin{cases} p_{2\text{ia}} e^{-jkx_b} + p_{2\text{ra}} e^{jkx_b} = p_{3\text{ia}} e^{-jkx_b} + p_{3\text{ra}} e^{jkx_b} \\ u_{2\text{ia}} e^{-jkx_b} + u_{2\text{ra}} e^{jkx_b} = u_{3\text{ia}} e^{-jkx_b} + u_{3\text{ra}} e^{jkx_b} \end{cases} \tag{7}$$

Substitution of Equation (2) into Equation (7) yields

$$\begin{cases} p_{3\text{ia}} = p_{2\text{ia}} \\ p_{3\text{ra}} = p_{2\text{ra}} \end{cases} \tag{8}$$

At $x = x_c$, the acoustic boundary condition is

$$\begin{cases} p_{3\text{ia}}e^{-jkx_c} + p_{3\text{ra}}e^{jkx_c} = p_{4\text{ia}}e^{-jkx_c} + p_{4\text{ra}}e^{jkx_c} \\ u_{3\text{ia}}e^{-jkx_c} + u_{3\text{ra}}e^{jkx_c} = u_{4\text{ia}}e^{-jkx_c} + u_{4\text{ra}}e^{jkx_c} \end{cases} \tag{9}$$

Substitution of Equation (2) into Equation (9) yields

$$\begin{cases} p_{4\text{ia}} = p_{3\text{ia}} \\ p_{4\text{ra}} = p_{3\text{ra}} \end{cases} \tag{10}$$

At $x = x_d$, the acoustic boundary condition is

$$\begin{cases} p_{4\text{ia}}e^{-jkx_d} + p_{4\text{ra}}e^{jkx_d} = p_{5\text{ia}}e^{-jkx_d} + p_{5\text{ra}}e^{jkx_d} \\ \left(u_{4\text{ia}}e^{-jkx_d} + u_{4\text{ra}}e^{jkx_d}\right)S_2 = \left(u_{5\text{ia}}e^{-jkx_d} + u_{5\text{ra}}e^{jkx_d}\right)S_1 \end{cases} \tag{11}$$

Substitution of Equation (2) into Equation (11) yields

$$\begin{cases} p_{5\text{ia}} = \dfrac{\left(1+S_2/S_1\right)p_{4\text{ia}}e^{-jkx_d} + \left(1-S_2/S_1\right)p_{4\text{ra}}e^{jkx_d}}{2e^{-jkx_d}} \\ p_{5\text{ra}} = \dfrac{\left(1-S_2/S_1\right)p_{4\text{ia}}e^{-jkx_d} + \left(1+S_2/S_1\right)p_{4\text{ra}}e^{jkx_d}}{2e^{jkx_d}} \end{cases} \tag{12}$$

At $x = L$, the acoustic boundary condition is

$$u_{5\text{ia}}e^{-jkL} + u_{5\text{ra}}e^{jkL} = j\omega d_B e^{j\phi_{AB}} \tag{13}$$

where d_B and ϕ_{AB} are the displacement amplitude of acoustic driver B and phase difference between two drivers. Equation (13) gives

$$p_{5\text{ia}}e^{-jkL} - p_{5\text{ra}}e^{jkL} = j\omega d_B \rho c e^{j\phi_{AB}} \tag{14}$$

Finally, by substituting Equations (4), (6), (8), (10) and (12) into Equation (14), we can obtain the solutions of $p_{1\text{ia}}$, $p_{1\text{ra}}$, $u_{1\text{ia}}$, $u_{1\text{ra}}$, $p_{2\text{ia}}$, $p_{2\text{ra}}$, $u_{2\text{ia}}$, $u_{2\text{ra}}$ and so on.

3.2 Acoustic field

Attention is focused on the acoustic field in the TA core (i.e., part 3 in Figure 3). It can be characterized by the standing-wave ratio G which is defined as

$$G = \frac{1+|r_p|}{1-|r_p|}, r_p = \frac{p_{3\text{ra}}}{p_{3\text{ia}}} \tag{15}$$

When $0 \le |r_p| \le 1$, $G \in [1, +\infty]$ with $G = 1$ corresponding to a pure right-propagating traveling wave and $G = +\infty$ corresponding to a pure standing wave. When $1 \le |r_p| < \infty$, $G \in [-\infty, -1]$ with $G = -1$ corresponding to a pure left-propagating traveling wave and $G = -\infty$ corresponding to a pure standing wave.

Figure 4 shows the dependence of $|p_{3ia}|$, $|p_{3ra}|$ and $|G|$ on f where the parameters in Table 1 are used in the calculation and $\phi_{AB} = 90°$. It is found that when f is below 292 Hz, $1 < |r_p| < \infty$. In particular, at $f = 110$ Hz, $G \approx -1$ which indicates that the acoustic field is dominated by a left-propagating traveling wave. Similarly, when f is between 292 Hz and 744 Hz, $0 < |r_p| < 1$. In particular, at $f = 563$ Hz, $G \approx 1$ which indicates that the acoustic field is dominated by a right-propagating traveling wave. When $f = 292$ Hz, $|r_p| \approx 1$, and $|G|$ has a very large value, indicating that the acoustic field is dominated by a standing wave.

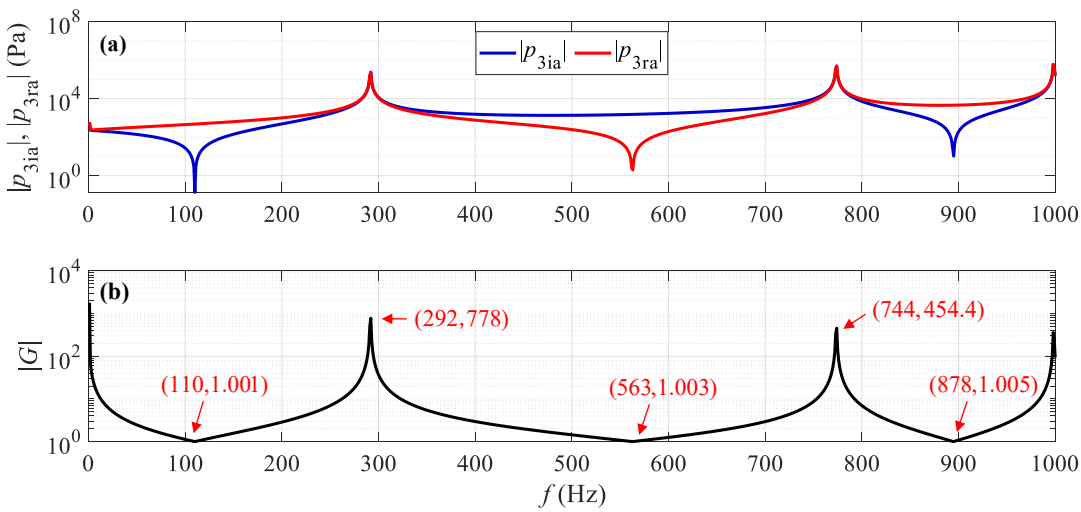

Figure 4. Dependence of $|p_{3ia}|$, $|p_{3ra}|$ and $|G|$ on f.

Figure 5 presents the distributions of acoustic pressure p, volume velocity U and their phase difference θ_{pU} at selected driving frequencies in Figure 4. The shaded area denotes the TA core region. In Figures 5(a) - 5(c), $f = 110$ Hz, corresponding to a left-propagating traveling wave in the core region. As a result, the curves of $|p|$ and $|U|$ are flat, and $\theta_{pU} = -180°$. In Figures 5(d) - 5(f), $f = 200$ Hz, corresponding to a hybrid standing-traveling wave in the core region. In this case, the curves of $|p|$ and $|U|$ are not flat with $|p|$ being minimum and $|U|$ being maximum in the middle of the core ($x = 0.25$ m). Due to the symmetry of the geometry and $|p_{3ra}/p_{3ia}| > 1$, θ_{pU} varies from -204° to -156° in the core region. In Figures 5(g) - 5(i), $f = 292$ Hz, corresponding to a standing wave in the core region. In this case, $|p|$ at $x = 0.25$ m reduces to near-zero (i.e., a node). Due to the symmetry, θ_{pU} is 90° in the left half of the core and changes to -90° in the right half. In Figures 5(j) - 5(l), $f = 400$ Hz, corresponding to a hybrid standing-traveling wave in the core region. The curves of $|p|$ and $|U|$ are similar to those at $f = 200$ Hz. Due to the symmetry and $|p_{3ra}/p_{3ia}| < 1$, θ_{pU} varies from 40° to -40° in the core region. In Figures 5(m) - 5(o), $f = 563$ Hz, corresponding to a

right-propagating traveling wave in the core region. The curves of $|p|$ and $|U|$ are flat, and $\theta_{pU} = 0°$ in the core region.

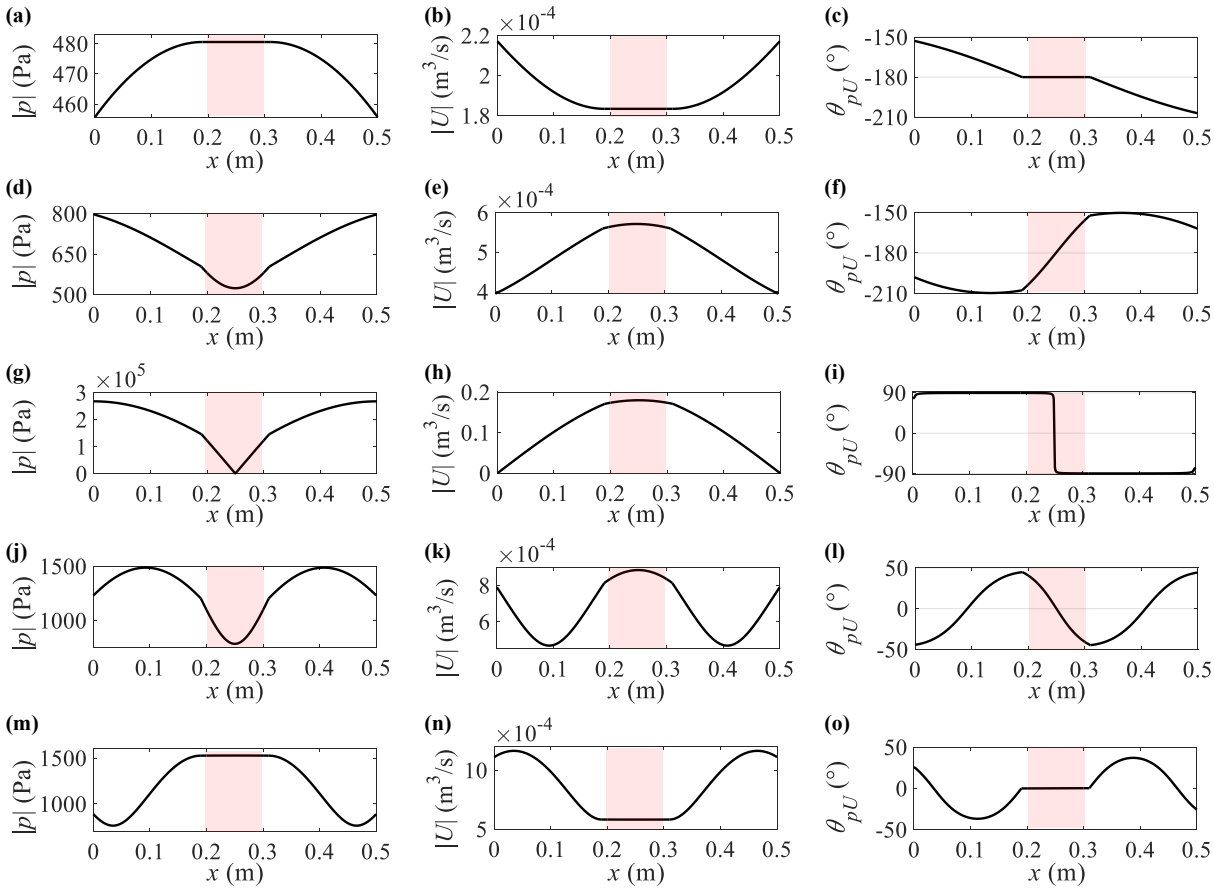

Figure 5. Acoustic field in the TAHP. In (a) - (c), f = 110 Hz; In (d) - (f), f = 200 Hz; In (g) - (i), f = 292 Hz; In (j) - (l), f = 400 Hz; In (m) - (o), f = 563 Hz. The shaded area denotes the TA core region.

Figure 6 shows the dependence of $f_{TW,L}$, f_{SW}, $f_{TW,R}$, $|p|_{TW,L}$ and $|p|_{TW,R}$ on ϕ_{AB}. $f_{TW,L}$, f_{SW} and $f_{TW,R}$ are frequencies at which the acoustic field in the core region is dominated by a left-propagating traveling wave, a standing wave and a right-propagating traveling wave, respectively. $|p|_{TW,L}$ and $|p|_{TW,R}$ are pressure amplitudes at $f_{TW,L}$ and $f_{TW,R}$, respectively. The reason why $|p|_{SW}$ is not displayed is that $|p|$ tends to infinity at f_{SW} due to acoustic resonance. In Figure 6(a), $f_{TW,L}$ increases from 17 Hz to 253 Hz, and $f_{TW,R}$ decreases from 746 Hz to 333 Hz as ϕ_{AB} increases from 15° to 165°. Due to the symmetry of geometry, f_{SW} remains unchanged at 292 Hz. In Figure 6(b), $|p|_{TW,L}$ increases from 86 Pa to 792 Pa, and $|p|_{TW,R}$ decreases from 2,738 Pa to 925 Pa as ϕ_{AB} increases from 15° to 165°. It is found that, $|p|_{TW,R}$ is always larger than $|p|_{TW,L}$ because $u = j\omega d_A$ is higher at $f_{TW,R}$ than at $f_{TW,L}$.

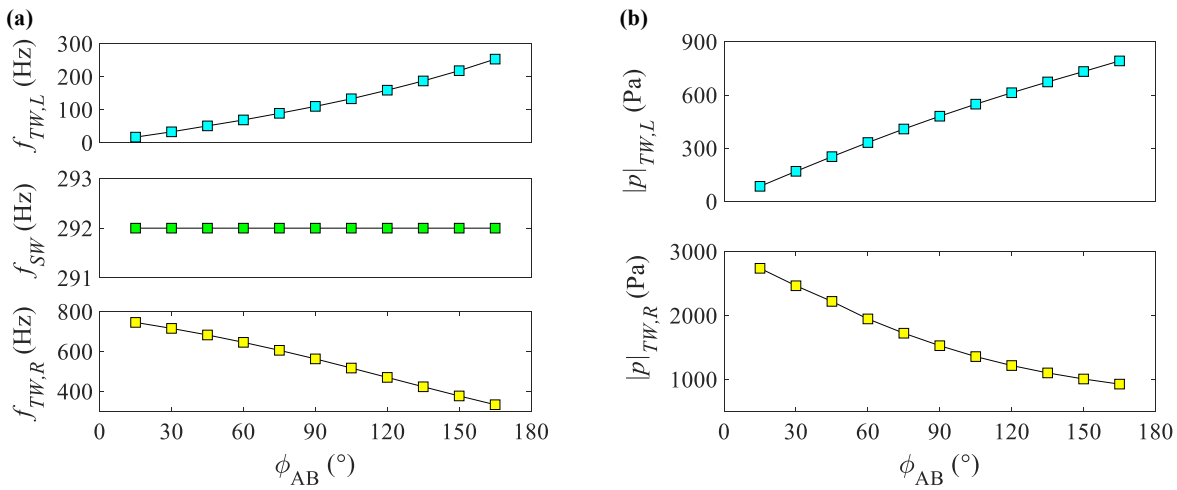

Figure 6. Dependence of $f_{TW,L}$, f_{SW}, $f_{TW,R}$, $|p|_{TW,L}$ and $|p|_{TW,R}$ on ϕ_{AB}.

4. Thermodynamic analysis

Following the acoustic analysis in Section 3, this section studies the thermal interaction between the oscillatory fluid and solid plates within the thermal boundary layers that stimulates a non-zero temperature difference between the core ends. The validation of the theoretical method in this section can be found in Appendix A.

4.1 Governing equations

In the linear thermoacoustic theory [1], the time-averaged total power $\dot{H}_2$ is often employed to study the energy flows inside a thermoacoustic system. It is expressed by

$$\dot{H}_2 = \dot{W}_2 + \dot{Q}_2 + \dot{Q}_{HC} + \dot{Q}_v \tag{16}$$

where $\dot{W}_2$, $\dot{Q}_2$, $\dot{Q}_{HC}$ and $\dot{Q}_v$ represent the time-averaged work flow, heat flow, energy flow through heat conduction and energy flow consumed by viscous shear, respectively. The subscript "2" denotes second-order, i.e., the product of two first-order quantities.

The first term $\dot{W}_2$ in Equation (16) can be written by [1]

$$\dot{W}_2 = \frac{1}{2}\int \Re[p_1\tilde{u}_1]dS = \frac{1}{2}\Re[p_1\tilde{U}_1] \tag{17}$$

where S is the cross-sectional area of the fluid channel, "1" denotes the first-order values, $\Re[\ ]$ and "~" signify the real value and conjugate of a complex quantity. The second term $\dot{Q}_2$ in Equation (16) is written as [1]

$$\dot{Q}_2 = \frac{1}{2}\rho_m T_m \int \Re[s_1 \tilde{u}_1] dS \tag{18}$$

with subscript "m" denoting the mean values. In Equation (18), the first-order complex entropy s_1 could be expressed as a function of first-order pressure p_1 and temperature T_1, i.e.,

$$s_1 = -\frac{p_1}{\rho_m T_m} + c_p \frac{T_1}{T_m} \tag{19}$$

where c_p is the isobaric specific heat. T_1 from the linear theory is [1]

$$T_1 = \frac{1}{\rho_m c_p}(1-h_k)p_1 - \frac{1}{j\omega}\frac{dT_m}{dx}\frac{(1-h_k)-Pr(1-h_v)}{(1-h_v)(1-Pr)}u_1 \tag{20}$$

where Pr denotes the Prandtl number. h_v and h_k are thermo-viscous functions [35] and written as

$$h_{v,k} = \cosh\left((1+j)y/\delta_{v,k}\right)/\cosh\left((1+j)r_h/\delta_{v,k}\right), \quad r_h = d_S/2 \tag{21}$$

with $y = 0$ being the centre of the fluid channel. $\delta_v = (2\mu/\rho_m\omega)^{0.5}$ is the viscous penetration depth and $\delta_k = (2\kappa/\rho_m c_p \omega)^{0.5}$ is the thermal penetration depth. μ and κ are dynamic viscosity and thermal conductivity of the working fluid. Substituting Equation (19) into Equation (18) yields

$$\dot{Q}_2 = -\frac{1}{2}\Re\left[f_k p_1 \tilde{U}_1\right] - \frac{1}{2}\rho_m c_p \frac{U_1^2}{S}\frac{dT_m}{dx}\Re\left[\frac{1}{j\omega}\frac{(1-f_k)-Pr(1-f_v)}{(1-f_v)(1-Pr)}\right] \tag{22}$$

where $f_{v,k} = \int h_{v,k} dS$. The third term $\dot{Q}_{HC}$ in Equation (16) includes the conduction of heat flow within the solid plates as well as in the gas between the solid plates. Since the thermal conductivity of gas is much smaller than that of solid, $\dot{Q}_{HC}$ is approximated by

$$\dot{Q}_{HC} = -S_{solid}\kappa_{solid}\frac{dT_m}{dx} \tag{23}$$

where S_{solid} and κ_{solid} denote the cross-sectional area and thermal conductivity of the solid plates. The last term $\dot{Q}_v$ in Equation (16) is usually negligible compared with $\dot{W}_2$ and $\dot{Q}_2$, and therefore omitted [1].

Substituting Equations (17), (22) and (23) into (16) yields

$$\frac{dT_m}{dx}=\frac{\dot{H}_2+\frac{1}{2}\left(\Re\left[f_k\right]-1\right)\left|p_1\right|\left|U_1\right|\cos\phi_{pU}-\frac{1}{2}\Im\left[f_k\right]\left|p_1\right|\left|U_1\right|\sin\phi_{pU}}{-S_{solid}\kappa_{solid}-\frac{1}{2}\rho_m c_p\frac{\left|U_1\right|^2}{S\omega}\Im\left[\frac{\left(1-f_k\right)-Pr\left(1-f_v\right)}{\left(1-f_v\right)\left(1-Pr\right)}\right]} \tag{24}$$

where $\Im[\ ]$signifies the imaginary value of a complex quantity. By integrating Equation (24) along x, we can obtain the temperature distribution within the TA core. It should be stressed that $\dot{H}_2$ in Equation (24) is constant in the TA core because there is negligible heat transfer between the TA core and its surroundings. Although $\dot{H}_2$changes inside the heat exchangers, its magnitude should be of the same order as $\dot{W}_2$ in the duct. In this work, we assume that $\dot{H}_2$ in the TA core is n times $\dot{W}_2$at $x = x_b$, i.e.,

$$\dot{H}_2\Big|_{core}=n\dot{W}_2\Big|_{x=x_b} \tag{25}$$

4.2 Temperature field

Figure 7 plots the temperature difference ΔT between the core ends at different f when ϕ_{AB} = 90° and n = 2. For simplicity, the temperature at the left end of the core is assumed unchanged at 300 K. First discussed are the temperature distributions in the TA core at $f_{TW,L}$ = 110 Hz, f_{SW}= 292 Hz and $f_{TW,R}$= 563 Hz where the acoustic field is dominated by a left-propagating, standing and right-propagating traveling wave, respectively. As shown in the insets, as x increases from 0.2 m to 0.3 m, T increases linearly at $f_{TW,L}$, first decreases then increases at f_{SW}, and decreases linearly at $f_{TW,R}$ in the core region. These temperature profiles agree with the conclusions made by Swift [11] that T in the TA core decreases along the propagation direction in a traveling-wave acoustic field but increases towards the pressure antinodes (at x = 0 and L) in a standing-wave acoustic field. It can be inferred from the insets that non-zero ΔT only exists in an acoustic field that contains a traveling-wave component. Second, it is interesting to notice that ΔT is maximum at f_{Max} = 282 Hz. At this frequency, the acoustic field contains both traveling- and standing-wave components. Thereby, the temperature distribution is jointly determined by both components, and its curve is parabolic as seen in the inset. The parabolic temperature profiles were also observed in experiments conducted by Widyaparaga [28] and El-Rahman [29]. Although the acoustic field has a small traveling-wave component at f_{Max}, its $|p|$ is large near f_{SW} (due to acoustic resonance), leading to a large value of ΔT. The same reasons apply to f_{Min} = 302 Hz at which the temperature profile is parabolic and ΔT is minimum. Finally, it is found that $|\Delta T|$ first decreases then increases as f increases

from 302 Hz to 650 Hz. The decrease of $|\Delta T|$ is related to the disappearance of acoustic resonance while the increase of $|\Delta T|$ is due to the increase of $|p|$ at higher frequencies.

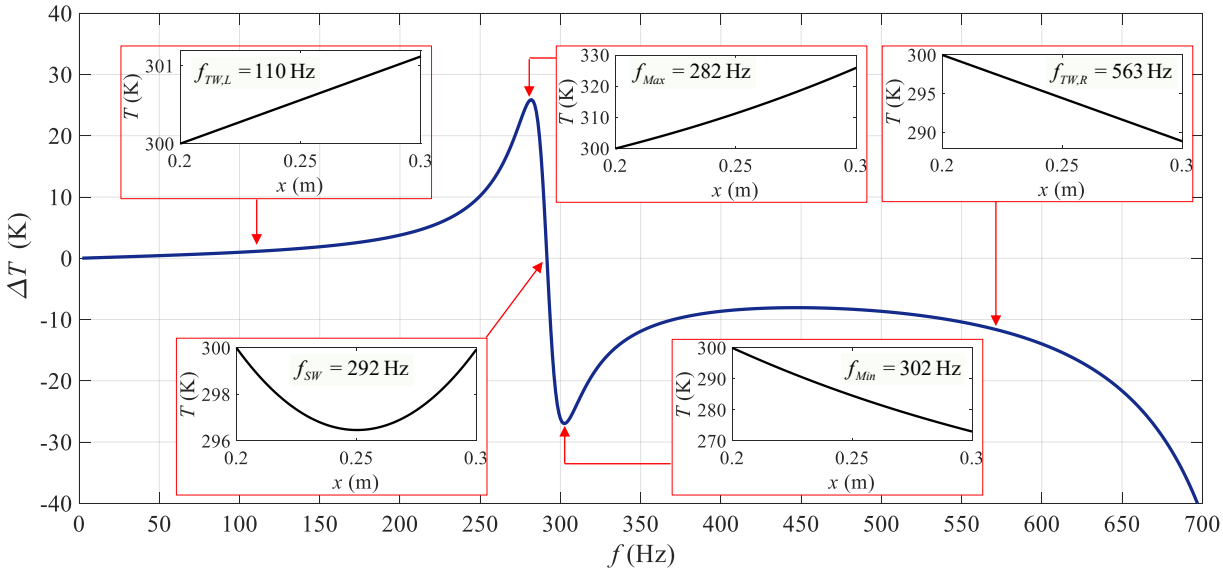

Figure 7. Temperature difference ΔT between the core ends at different f when $\phi_{AB} = 90°$ and $n = 2$.

Figure 7 demonstrates that acoustic resonance should be utilized to achieve a large $|\Delta T|$. Specifically, f of the acoustic drivers should be tuned near f_{Max} or f_{Min} (but not at f_{SW}). Hence, the larger $|f_{Max}-f_{Min}|$ is, a wider bandwidth for a large $|\Delta T|$ will exist. Through calculations, we find that f_{Max} and f_{Min} are hardly affected by n but are greatly influenced by ϕ_{AB}. Figure 8 shows the dependence of f_{Max} and f_{Min} on ϕ_{AB}. It is found that as ϕ_{AB} increases, f_{Max} increases but f_{Min} decreases. $|f_{Max}-f_{Min}|$ is larger at smaller ϕ_{AB} which indicates a wider bandwidth to obtain a large $|\Delta T|$. Following Figure 8, we proceed to investigate the effects of n and ϕ_{AB} on ΔT. Figure 9 displays the contours of $\Delta T_{TW,L}$, ΔT_{Max}, ΔT_{Min} and $\Delta T_{TW,R}$, representing ΔT at $f_{TW,L}$, f_{Max}, f_{Min} and $f_{TW,R}$. It can be found from Figure 9 that $|\Delta T|$ at f_{Max} and f_{Min} are way larger than those at $f_{TW,L}$ and $f_{TW,R}$. This further elucidates that acoustic resonance is pivotal for the TAHP to achieve a large $|\Delta T|$. Moreover, $|\Delta T|$ in Figure 9(d) is larger than those in Figure 9(a) due to higher values of $f_{TW,R}$ and $|p|_{TW,R}$ (see Figure 6). In general, $|\Delta T|$ increases with the increase of n. $|\Delta T_{Max}|$ and $|\Delta T_{Min}|$ increases with increasing ϕ_{AB}. As ϕ_{AB} increases, $|\Delta T_{TW,L}|$ increases but $|\Delta T_{TW,R}|$ decreases: these trends are consistent with f and $|p|$ versus ϕ_{AB} in Figure 6.

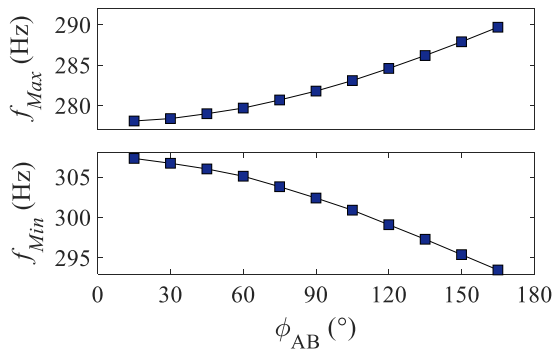

Figure 8. Dependence of f_{Max} and f_{Min} on ϕ_{AB}.

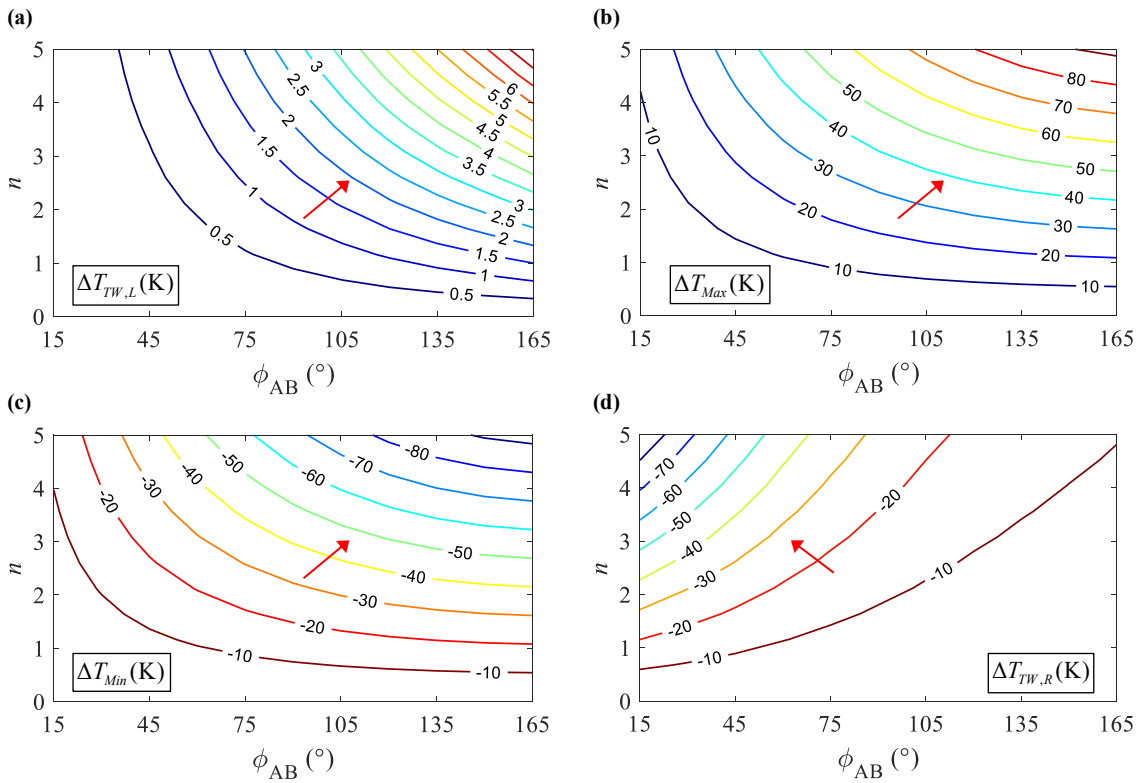

Figure 9. Contours of (a) $\Delta T_{TW,L}$, (b) ΔT_{Max}, (c) ΔT_{Min} and (d) $\Delta T_{TW,R}$. The arrows point to the direction in which $|\Delta T|$ increases.

5. Conclusions

This study focused on the operation characteristics of a thermoacoustic heat pump (TAHP) that is driven by two acoustic drivers and has the inherent merit of compactness. The working principle of the dual-acoustic-driver TAHP was first described and its differences from traditional Stirling heat pumps were briefly introduced. Subsequently, theoretical methods were proposed to calculate the acoustic and temperature fields in the core region. Parametric studies were performed to investigate the effect of

acoustic drivers on the acoustic and thermal characteristics of the TAHP. We make the following conclusions from this study.

(1) Active control of the acoustic field inside the TAHP can be realized by changing the operating parameters of the acoustic drivers. Characterized by the standing-wave ratio, the acoustic field in the core region could be dominated by a left-propagating traveling wave, a right-propagating traveling wave, a standing wave, or a hybrid standing-traveling wave as the driving frequency changes.

(2) The temperature field in the core region is strongly affected by the acoustic field. Heat is pumped to the right (or left) for a left-propagating (or right-propagating) traveling wave, and the temperature distribution along the TA core is linear. However, for a standing wave, heat is pumped from the middle to both ends, and the temperature profile has a "U" shape. For a hybrid standing-traveling wave, the heat pumping process is jointly determined by its standing- and travelling-wave components, and the resultant temperature profile is parabolic.

(3) Non-zero temperature difference ΔT between the core ends only exists in acoustic fields containing a traveling-wave component. However, $|\Delta T|$ is small in acoustic fields dominated by traveling waves since the pressure amplitude $|p|$ is small. Although $|p|$ is high at acoustic resonance, $|\Delta T|$ at resonance frequencies is still small (approaches zero) due to the symmetry of the U-shaped temperature profile in the core region. Therefore, to obtain a larger $|\Delta T|$, the acoustic drivers should be driven near resonance frequencies (e.g., at f_{Max} or f_{Min}) at which the acoustic field is hybrid and $|p|$ is large.

Finally, it is worth mentioning that the theoretical methods in this study are valid in the linear regime. These models, although simplified, provide a valuable theoretical tool to study the working mechanism of the dual-acoustic-driver TAHP in addition to the numerical tools such as DeltaEC [36] and Sage [37] that were usually adopted in the literature. Prospective research will involve the development of nonlinear models and the validation of theoretical methods through CFD (computational fluid dynamics) simulations and experimental measurements.

Acknowledgements

Financial support from the Fundamental Research Funds for the Central Universities (no. 3203002101C3) is acknowledged.

Appendix A. Comparison with experiments

The experimental data recently reported by El-Rahman et al. [29] was used to validate the theoretical methods in this study. In their study, the configuration of the thermoacoustic device tested resembles the dual-acoustic-driver TAHP in Figure 1 except that the heat exchangers were omitted. The driving

frequency of the piston was 42 Hz and the phase difference between the two pistons was adjusted. Two pressure transducers were employed to measure the pressure amplitude close to the oscillation pistons and two thermocouples were used to measure the temperature difference at the core ends.

Figures A1(a) and A1(b) display the distribution of pressure amplitude $|p|$ at ϕ_{AB} = 180° and the dependence of temperature difference ΔT on ϕ_{AB}, respectively. The discrete squares are those measured in the experiment and solid lines represent theoretical predictions by substituting the geometrical and thermophysical parameters in the experiment into the theoretical analyses. Since there are no heat exchangers in the experiment, n = 1 is selected. As seen in Figure A1(a), the values of pressure amplitudes from the experiment and the theoretical estimate are close. $|p|$ in the experiment are slightly lower than the theoretical estimates due to the negligence of viscous losses in the acoustic model and other factors such as possible gas leaks caused by the thin air gap between the cylinder and piston [38]. In Figure A1(b), an overall agreement is achieved between the experimental measurements and theoretical estimates of ΔT at selected ϕ_{AB}. The deviations of experimental data from the theory are possibly caused by the nonlinear effects such as harmonics, turbulence, mass streaming, etc [29].

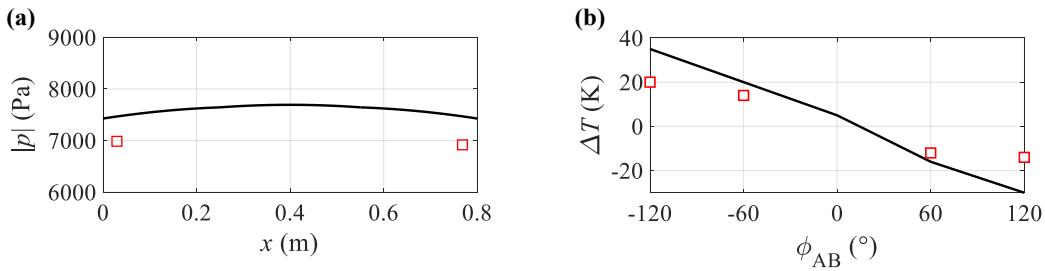

Figure A1. Comparison between the theoretical predictions (solid lines) the experimental data (discrete squares) reported by El-Rahman et al. [29]. (a) Distribution of pressure amplitude at ϕ_{AB} = 180°. (b) Dependence of temperature difference ΔT on ϕ_{AB}.

References

[1] Swift GW. Thermoacoustics: A unifying perspective for some engines and refrigerators: Springer; 2017.

[2] Jin T, Huang J, Feng Y, Yang R, Tang K, Radebaugh R. Thermoacoustic prime movers and refrigerators: Thermally powered engines without moving components. Energy. 2015;93:828-53.

[3] Yang R, Blanc N, Ramon GZ. Environmentally-sound: An acoustic-driven heat pump based on phase change. Energy Conversion and Management. 2021;232:113848.

[4] Chen G, Tang L, Mace B, Yu Z. Multi-physics coupling in thermoacoustic devices: A review. Renewable and Sustainable Energy Reviews. 2021;146:111170.

[5] Wang K, Sun DM, Zhang J, Zou J, Wu K, Qiu LM, et al. Numerical simulation on onset characteristics of traveling-wave thermoacoustic engines based on a time-domain network model. International Journal of Thermal Sciences. 2015;94:61-71.

[6] Zink F, Waterer H, Archer R, Schaefer L. Geometric optimization of a thermoacoustic regenerator. International Journal of Thermal Sciences. 2009;48:2309-22.

[7] Piccolo A. Optimization of thermoacoustic refrigerators using second law analysis. Applied energy. 2013;103:358-67.

[8] Merkli P, Thomann H. Thermoacoustic effects in a resonance tube. Journal of Fluid Mechanics. 1975;70:161-77.

[9] Wheatley J, Hofler T, Swift G, Migliori A. An intrinsically irreversible thermoacoustic heat engine. The Journal of the Acoustical Society of America. 1983;74:153-70.

[10] Hofler TJ. Thermoacoustic refrigerator design and performance. 1986.

[11] Swift GW. Thermoacoustic engines. The Journal of the Acoustical Society of America. 1988;84:1145-80.

[12] Rott N. Thermoacoustics. Advances in applied mechanics. 1980;20:135-75.

[13] Yazaki T, Biwa T, Tominaga A. A pistonless Stirling cooler. Applied Physics Letters. 2002;80:157-9.

[14] Tijani M, Zeegers J, De Waele A. Design of thermoacoustic refrigerators. Cryogenics. 2002;42:49-57.

[15] Luo E, Dai W, Zhang Y, Ling H. Thermoacoustically driven refrigerator with double thermoacoustic-Stirling cycles. Applied physics letters. 2006;88:074102.

[16] De Blok K. Low operating temperature integral thermo acoustic devices for solar cooling and waste heat recovery. Journal of the Acoustical Society of America. 2008;123:3541.

[17] https://www.soundenergy.nl/.

[18] Biwa T, Ueda Y, Nomura H, Mizutani U, Yazaki T. Measurement of the Q value of an acoustic resonator. Physical Review E. 2005;72:026601.

[19] Chen G, Tang L, Mace BR. Modelling and analysis of a thermoacoustic-piezoelectric energy harvester. Applied Thermal Engineering. 2019;150:532-44.

[20] Chen G, Wang Y, Tang L, Wang K, Yu Z. Large eddy simulation of thermally induced oscillatory flow in a thermoacoustic engine. Applied Energy. 2020;276:115458.

[21] Wheatley J, Hofler T, Swift G, Migliori A. Experiments with an intrinsically irreversible acoustic heat engine. Physical Review Letters. 1983;50:499.

[22] Yu Z, Jaworski AJ, Backhaus S. Travelling-wave thermoacoustic electricity generator using an ultra-compliant alternator for utilization of low-grade thermal energy. Applied Energy. 2012;99:135-45.

[23] Zhang X, Chang J, Cai S, Hu J. A multi-stage travelling wave thermoacoustic engine driven refrigerator and operation features for utilizing low grade energy. Energy Conversion and Management. 2016;114:224-33.
[24] Xu J, Luo E, Hochgreb S. Study on a heat-driven thermoacoustic refrigerator for low-grade heat recovery. Applied Energy. 2020;271:115167.
[25] Poignand G, Lotton P, Penelet G, Bruneau M. Thermoacoustic, small cavity excitation to achieve optimal performance. Acta Acustica united with Acustica. 2011;97:926-32.
[26] Poignand G, Podkovskiy A, Penelet G, Lotton P, Bruneau M. Analysis of a coaxial, compact thermoacoustic heat-pump. Acta Acustica united with Acustica. 2013;99:898-904.
[27] Widyaparaga A, Hiromatsu T, Koshimizu T, Deendarlianto D, Kohno M, Takata Y. Thermoacoustic heat pumping direction alteration by variation of magnitude and phase difference of opposing acoustic waves. Applied Thermal Engineering. 2016;101:330-6.
[28] Widyaparaga A, Hiromatsu T, Kohno M, Takata Y. Acoustic field alteration in a 100 Hz dual acoustic driver straight tube travelling wave thermoacoustic heat pump for thermoacoustic heat transport control. International Journal of Heat and Mass Transfer. 2020;151:119274.
[29] Abd El-Rahman AI, Abdelfattah WA, Abdelwahed KS, Salama A, Rabie A, Hamdy A. A compact standing-wave thermoacoustic refrigerator driven by a rotary drive mechanism. Case Studies in Thermal Engineering. 2020;21:100708.
[30] Ramadan IA, Bailliet H, Poignand G, Gardner D. Design, manufacturing and testing of a compact thermoacoustic refrigerator. Applied Thermal Engineering. 2021:116705.
[31] Timmer MA, de Blok K, van der Meer TH. Review on the conversion of thermoacoustic power into electricity. The Journal of the Acoustical Society of America. 2018;143:841-57.
[32] Chen G, Xu J. Acoustic characteristics of looped-tube thermoacoustic refrigerators with external and in-built acoustic drivers: A comparative study. The Journal of the Acoustical Society of America. 2021;150:4406-16.
[33] Chen G, Tang L, Yu Z, Mace B. Mode transition in a standing-wave thermoacoustic engine: A numerical study. Journal of Sound and Vibration. 2021:116119.
[34] Ceperley PH. A pistonless Stirling engine—The traveling wave heat engine. The Journal of the Acoustical Society of America. 1979;66:1508-13.
[35] Arnott WP, Bass HE, Raspet R. General formulation of thermoacoustics for stacks having arbitrarily shaped pore cross sections. The Journal of the Acoustical Society of America. 1991;90:3228-37.
[36] Ward B, Clark J, Swift G. Design Environment for Low (amplitude Thermoacoustic Energy Conversion DeltaEC Version 6.3 b11 Users Guide. Los Alamos national laboratory. 2012.

[37] Gedeon D. Sage: object-oriented software for cryocooler design. Cryocoolers 8: Springer; 1995. p. 281-92.

[38] Penelet G, Watanabe T, Biwa T. Study of a thermoacoustic-Stirling engine connected to a piston-crank-flywheel assembly. The Journal of the Acoustical Society of America. 2021;149:1674-84.